Flow separation from polygonal cylinders in an incident flow

Esmaeel Masoudi [*], David Sims-Williams [†] and Lian Gan [‡]
Department of Engineering, Durham University, Durham, DH1 3LE, United Kingdom

In this paper, we carry out large eddy simulation of incident flow around polygonal cylinders of side number $N = 5-8$ at Reynolds number $Re = 10^4$. In total, six incidence angles (α) are studied on each polygon between the face and the corner orientations, thus covering the entire α spectrum. It is found that the separated shear layers behind the cylinders are highly dynamic, manifesting a flapping motion with frequency matching the Strouhal frequency and strength varying significantly at different incidence angles. The energy of the flapping motion is found to be a significant factor influencing the dynamic flow separation behavior, the distribution of the separation points, and features of the time mean shear layer, such as characteristic length and width. Equations for the separation points are analytically derived and are found to be consistent with available experimental results. The time mean penetration distance of the separated shear layers on the top and bottom of the cylinders is found to be a robust scaling factor for the aerodynamic forces and the near-wake length scales. Based on this, a wake deflection angle is proposed, which is demonstrated to be a universal scaling factor for lift, drag, and Strouhal number, working for all available polygonal and circular cylinder data. Finally, the critical separation angle is empirically derived for the condition at which the Strouhal number is a maximum and drag is minimized.

I. INTRODUCTION

Flow around a single stationary bluff body has been studied extensively for more than 200 years, especially since the discovery of Kármán vortex streets. Previous research has mostly focused on the flow around circular cylinders and a few other regular-shaped bluff bodies such as triangular, rectangular, and square cylinders; see Williamson [1], Zdravkovich [2], Matsumoto [3], Thompson *et al.* [4]. In addition to the effect of the Reynolds number, special attention has been paid to the periodic vortex shedding process, usually quantified by Strouhal number St, the aerodynamic forces including the time mean drag coefficient C_D, and the fluctuating lift coefficient, as well as the evolution of the vortex driven wake. The Reynolds number is usually defined by the streamwise projected characteristic length scale of the bluff body D, the incoming free stream flow velocity U_∞, and the kinematic viscosity of the working fluid ν, i.e., $Re = U_\infty D/\nu$. The behavior of these physical processes are all fundamentally determined by the flow separation from the surface of the bluff body and hence the roll-up into vortex streets from the separated shear layers [2].

Flow past polygonal cylinders of side number N generally resembles the flow around circular cylinders, especially in terms of the formation of Kármán vortex streets for $Re \gtrsim O(10^2)$. However, because of their quasiaxisymmetric shape, the local boundary layer separation behavior exhibits

---
[*]esmaeel.masoudi@durham.ac.uk

[†]d.b.sims-williams@durham.ac.uk

[‡]Corresponding author: lian.gan@durham.ac.uk

significant N dependence. For small N, the flow typically separates from a particular corner (edge along the spanwise direction) on the top and bottom side of the cylinder, due to the abrupt change of local pressure. These separation points are relatively insensitive to Re. In some cases, the separated flow may reattach and then separate again from a downstream corner. Even though the corner angle and the length of the face (for a given cylinder diameter) are both a monotonic function of N, the exact pressure gradient and the associated boundary layer reattachment behavior (that determine the overall aerodynamic performance and the near-wake flow structure) are strongly nonmonotonic with side number N.

Until recently, studies on flow around polygonal cylinders of $N > 4$ remained scattered, even though cylinders of $N = 3$ and 4 (triangular and square cylinders) have been well investigated ([5–12]). Tian and Li [13] studied a cylinder of $N = 24$ in a low-speed wind tunnel and found a much lower critical transitional Reynolds number and a 40% lower drag with a lower level of fluctuation compared to a circular cylinder under similar flow conditions. Tian and Wu [14] theoretically investigated inviscid flow and low-Reynolds number (Re < 200) viscous flow around two-dimensional polygonal cylinders at corner orientation for even values of N. Using conformal mapping, they showed that for the inviscid flow case, the global pressure difference along the surface is inversely proportional to the side number for sufficiently large values of N. For the viscous flow case, however, by deriving the relation between the first critical Re and N, they found that this Re monotonically decreases for steady flows and increases for unsteady flows as a function of N. Using direct numerical simulations at Re $= 100, 500, 1000$, Khaledi and Andersson [15] studied flow past hexagonal cylinders ($N = 6$) in principal orientations, viz. either a surface or a corner faces the incoming flow direction. They found that St is slightly higher in face orientation. They further explained that the Kármán vortices roll up closer to the body in the case of face orientation which results in a shorter formation region and a higher St. They concluded that the wake behind the face or corner oriented hexagonal cylinders resembles that of the square cylinder in the same orientation and therefore the aft-body plays a minor role. Lee *et al.* [16] conducted two-dimensional numerical simulations to investigate flow over regular and isotoxal-star polygonal cylinders at Re $= 150$ and suggested that isotoxal-star polygons exhibit higher lift and drag compared to regular polygons.

In a wind tunnel experiment, Xu *et al.* [17] systematically studied the aerodynamic performance and flow separation characteristics on polygonal cylinders of $N = 2 \sim 8, 12, 16$ at their principal orientations over $10^4 \leqslant$ Re $\leqslant 10^5$, utilising a combination of force measurement, flow visualisation and planar particle image velocimetry (PIV). They found that flow transition to turbulence does not occur for polygons of $N \leqslant 8$, reflected by Re insensitive C_D and St values, as well as the flow separation point location. They also proposed a formula for the *corrected* separation angle ξ measured from the windward stagnation point (WSP), in the absence of the flow transition effect, as

$$\xi = \frac{180}{\pi} \times \begin{cases} \frac{\pi}{2} - \left(p - \frac{1}{2}\right)\left(\frac{2\pi}{N}\right), & \text{corner orientation} \\ \frac{\pi}{2} - (q - 1)\left(\frac{2\pi}{N}\right), & \text{face orientation,} \end{cases} \tag{1}$$

where $p = \lceil (N - 2)/4 \rceil$ and $q = \lceil N/4 \rceil$, $\lceil \cdot \rceil$ being the nearest larger integer.

Xu *et al.* [17] further suggested that, for polygons of $N \geqslant 12$, flow transition to turbulence does occur in the tested Re range, and the flow dynamics starts to approach that of the circular cylinder asymptotically. As the number of corners is large in these cases, the difference between the corner and the face radii is small, hence the corners could be treated as roughness elements on the surface of a circular cylinder. Re dependence then becomes important, similar to the critical Re effect on a rough surface circular cylinder. They also showed that, at the two principal orientations, St and C_D values are inversely related (similar to the case for circular cylinders).

In a subsequent PIV investigation of the wake flow behind polygonal cylinders, Wang *et al.* [18] showed that the vortex formation mechanism is well reflected by the characteristic length scales in the near-field wake, which includes but is not limited to the length of the reversed flow zone, the recirculation bubble width, the classical vortex formation length, and the characteristic wake

width. Based on empirical relations between these length scales and various kinematic and dynamic quantities, they suggested that the behavior of the wake behind the polygonal cylinder could be unified to that behind the circular cylinder. In a continuing wind tunnel PIV experiment, Wang *et al.* [19] further presented detailed data of the wake of polygonal cylinders $3 \leqslant N \leqslant 16$ with face and corner orientations at $\mathrm{Re} = 1.6 \times 10^4$, and studied the dependence on N and the orientation of the mean velocity and Reynolds stress distribution, as well as coherent vortex structures in the near wake. They showed that the circulation of each shed vortex grows to their maximum value at the vortex formation point measured by formation length and then decays downstream due to the combined effect of viscous dissipation and vortex cancellation.

In a recent study, Masoudi *et al.* [20] investigated the aerodynamic forces and near wake flow fields behind polygonal cylinders of $N = 5 \sim 8$ subjected to the effect of incidence angle α with respect to (w.r.t.) U_∞ at a fixed Reynolds number of $\mathrm{Re} = 10^4$ using three-dimensional large eddy simulation (LES). Based on the time mean spanwise vorticity fields, they defined a mean shear layer length L_ω considering an arbitrary intensity threshold, and found it to be a reasonable scaling factor for the investigated aerodynamic properties including St, C_D, and base pressures. Furthermore, they showed that due to the asymmetric nature of polygonal cylinders in off-principal orientations, the time mean wake is also asymmetric, resulting in a nonzero mean lift. The well-established empirical relationship between St and C_D for general bluff body shapes that has been proposed by many researchers including but not limited to Hoerner [21], Ahlborn *et al.* [22], Alam and Zhou [23], and for polygons at principal orientations Xu *et al.* [17], is found to be valid for polygonal cylinders in incident incoming flows.

In the present paper, we address the dependence on incidence angle of the instantaneous separation dynamics of shear layers from polygonal cylinders of $N = 3 \sim 8$ and its signature in the time mean manifestation and the corresponding vorticity field in the near wake. In particular, we focus on the effect of an observed strong flapping motion of the separated shear layers and its impact on fundamental aerodynamic forces through a proper scaling parameter associated with the wake flow. The critical separation angle is also empirically derived to predict the minimum C_D and maximum St condition.

II. COMPUTATIONAL MODELING AND NUMERICAL SETUP

A. Computational domain and boundary conditions

We perform three-dimensional LES for polygonal cylinders of side number $N = 5, 6, 7, 8$ in an incident incoming flow directions. Six equal-spaced angles of attack α are considered for each cylinder rotating clockwisely w.r.t. the incoming flow from the corner ($\alpha = 0°$) to the face ($\alpha = 180°/N$) orientation. This effectively covers all possible orientations for a given polygon. Since in this way the absolute step size $\Delta\alpha$ decreases for increasing N, a scaled incidence angle $\alpha^* = \alpha/(180/N)$ is utilized. Following this definition, $\alpha^* = 0$ and $\alpha^* = 1$ correspond to corner and face orientations, respectively. The scaled step size $\Delta\alpha^*$ is thus fixed at 0.2 between the two principal orientations.

The computational domain is sketched in Fig. 1. R_c and R_i denote the circum-circle and in-circle radius of the polygon and the corresponding diameters are D_c and D_i. In this paper, R_i is chosen to be constant for all the polygonal cylinders, which results in a constant $\mathrm{Re} = 1 \times 10^4$ based on D_i. To investigate the effect of α, a body-fitted O-type structured grid is applied to ensure grid orthogonality, which is commonly adopted for similar problems [24–32, among others]. The domain outer boundary is set at $20D_i$ from the cylinder center, where the origin of the coordinate system is placed. The cylinder axis is aligned with the z axis and the incoming flow velocity U_∞ is set at the desired α w.r.t. the x' axis.

The number of cells in the radial and circumferential directions are denoted as N_r and N_θ, respectively, with $216 \leqslant N_r = N_\theta \leqslant 224$. The exact integer for N_θ depends on N, so the number of cell divisions on each edge of a given polygon is the same. The grid size grows exponentially
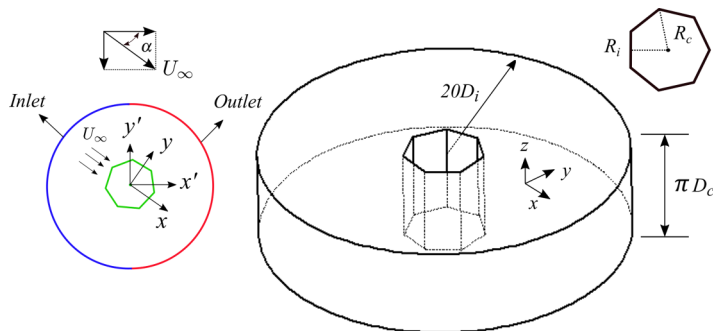
FIG. 1. Computational domain and problem configuration. Not to scale. The coordinate system $x' - y'$ is fixed in space, which bisects the outer surface to the inlet and the outlet and sets the inflow components, $x - y$ is aligned with the incidence angle α dependent U_∞ direction.

in the radial direction (r) from the body surface and is uniformly spaced in the circumferential direction (θ) and the spanwise direction (z). The growth rate in the r direction is set such that the maximum y^+ value is below unity, where $y^+ = y u_\tau / \nu$ with $u_\tau = \sqrt{\tau_w/\rho}$ and τ_w being the wall shear stress.

Following a number of previous three-dimensional LES studies of cylinders at various Re [see Refs. 26,31–37, for example], a spanwise length of $L_z = \pi D_c$, and the number of cells $N_z \approx 48 \times D_c/D_i$ are utilized, with periodic boundary conditions applied at both end surfaces of the domain. This is to achieve satisfactory accuracy of the resulting aerodynamic forces and the wake flow patterns and at the same time to minimize unrealistic topology associated with the application of the periodic boundary conditions and to prevent periodic artifacts. The inlet and outlet surfaces are indicated in Fig. 1. At the inlet surface, constant and uniform free stream flow velocity U_∞ is imposed accordingly to the α condition. At the outlet surface, a Neumann boundary condition is imposed to avoid flow reflection.

B. The LES solver

The governing equation for the current constant Smagorinsky (SMG) LES simulations, with kernel $G = G(x, \Delta)$ and Δ being the grid filter width, is:

$$\frac{\partial \bar{u}_i}{\partial x_i} = 0, \tag{2}$$

$$\frac{\partial \bar{u}_i}{\partial t} + \frac{\partial \bar{u}_i \bar{u}_j}{\partial x_j} = -\frac{1}{\rho}\frac{\partial \bar{p}}{\partial x_i} + \frac{\partial}{\partial x_j}\left[\nu\left(\frac{\partial \bar{u}_i}{\partial x_j} + \frac{\partial \bar{u}_j}{\partial x_i}\right) + \tau_{ij} \right], \tag{3}$$

where $\bar{u}$ and $\bar{p}$ are the filtered velocity and filtered pressure, respectively. In the spatially filtered Navier-Stokes equations, the stress term $\tau_{ij} = \overline{u_i u_j} - \bar{u}_i \bar{u}_j$ is modeled using the eddy-viscosity type subgrid scale (SGS) model of SMG [38], which is based on Boussinesq's assumption,

$$\tau_{ij} - \frac{2}{3}k_t \delta_{ij} = -2\nu_t\left(\bar{S}_{ij} - \frac{1}{3}\bar{S}_{kk}\delta_{ij}\right), \tag{4}$$

$$\bar{S}_{ij} = \frac{1}{2}\left(\frac{\partial \bar{u}_i}{\partial x_j} + \frac{\partial \bar{u}_j}{\partial x_i}\right), \tag{5}$$

where $\bar{S}_{ij}$ is the rate of strain tensor computed from the resolved scales; ν_t and k_t are SGS viscosity and turbulent kinetic energy respectively; see Fureby et al. [39] for a comprehensive review of all SGS models.
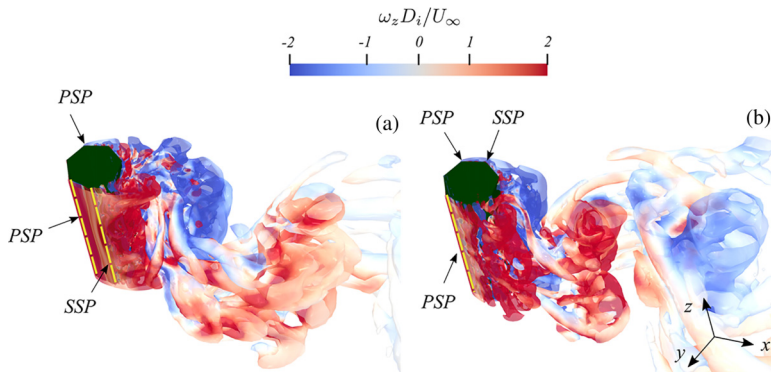
FIG. 2. Instantaneous fully developed wake over the full span L_z of the $N = 7$ cylinder at $\alpha^* = 0$. Iso-surface is based on Q criterion at an arbitrary level and is colored by the spanwise vorticity. (a) and (b) are at $t^* = tU_\infty/D_i = 325$ and $t^* = 329$, roughly corresponding to arbitrarily defined wake phase angle $\phi = \pi/2$ and $\phi = 3\pi/2$, respectively. The highlighted separation lines are the edges where primary (PSP) and secondary flow separation (SSP) occur in each case.

In the algebraic SMG model [38], ν_t and k_t are calculated explicitly under the assumption of local equilibrium balance between production and dissipation of k_t. The SMG coefficient $C_s = 0.1$ is adopted based on several validated studies of flow around circular cylinders [25,26,28–30, among others], and a near-wall damping function suggested by Van Driest [40] is implemented to improve SGS near-wall behavior [27,28,30],

$$\Delta = \min\left(\frac{k_v}{C_\Delta}, \Delta\right) y \left[1 - \exp\left(\frac{-y^+}{25}\right)\right],$$ (6)

where the Von Kármán constant $k_v = 0.4187$ and model constant $C_\Delta = 0.158$. No wall function is used in grid scale and $y^+ < 1$ effectively imposed on the cylinders with appropriate grid growth rate as described earlier.

In this paper, LES simulations were implemented in OPENFOAM with backward second-order time integration scheme. The predictor-corrector PISO (pressure-implicit with splitting of operators) loop is used to decouple and iteratively solve the pressure and velocity fields. Three PISO correctors are used for each time step to minimize uncertainty of the final results. The pressure is solved by a geometric agglomerated algebraic multigrid solver. A dynamic time step is utilized to keep the maximum Courant number of unity all over the domain. Simulations were carried out by a supercomputer with 120 processors.

A mesh sensitivity study and validation of the simulation results with experimental data ([17]) are detailed in Masoudi *et al.* [20]. Analysis also shows that the adopted mesh and numerical scheme in this study resolve more than 90% of the turbulent kinetic energy (except near the separation points, at which it is roughly 80%) and therefore the current LES is considered well resolved [41]. For all 24 cases (four polygons, six α^* each), simulation continued past the transient period and ensured that at least 30 fully developed vortex shedding cycles are acquired for evaluating time mean quantities.

III. RESULTS AND DISCUSSIONS

Figure 2 shows the isosurfaces of fully developed instantaneous velocity fields in the wake of the heptagonal cylinder ($N = 7$) at corner orientation ($\alpha^* = 0$). Here, PSP stands for the primary separation point, which is defined as the corner at which the flow separates for the first time, and SSP the secondary separation point, which is the corner from which the reattached flow separates. The exact reattachment location of the shear layer, if it occurs, usually is somewhere on the surface between the PSP and SSP, rather than exactly at the SSP itself. The Kármán vortex shedding pattern
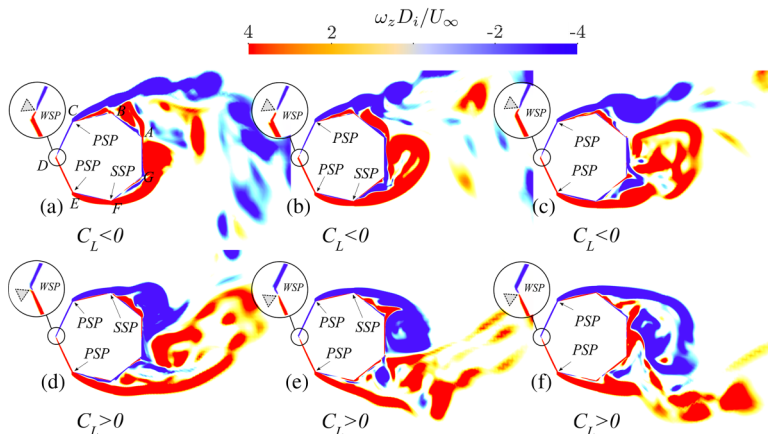
FIG. 3. Instantaneous spanwise vorticity fields at midspan of $N = 7$ $\alpha^* = 0$. (a) $t^* = 325$, matching Figs. 2(a) and 2(b)–2(e) correspond to $t^* + 1$, $t^* + 2$, $t^* + 3$, $t^* + 4$, and $t^* + 5$, respectively. It covers 5/8 of a shedding cycle, i.e., $0 \lesssim \phi \lesssim 5\pi/4$. The region around the leading corner is magnified to assist visualization of the location of the windward stagnation point (WSP), which is fluctuating approximately in phase with the vortex shedding. The sign of the instantaneous lift coefficient C_L and the separation points (PSP, SSP and PSP+SSP) are depicted for each case.

is evident and the high level of turbulence is reflected by the irregular isosurface pattern. The flow in the wake also manifests strong inhomogeneity along the spanwise (z) direction. However, owing to the low N number and the subcritical Re condition investigated in the current paper (see Ref. [17]), over the spanwise range L_z, flow separation is found to always occur along the same edge. The local vortex shedding is always in phase and the local separated shear layer (unsteady) deflection angle is fairly constant along the span. That is, the separation behavior is largely spanwise invariant, especially for the time mean quantities over the near-field wake region, which are constant in the spanwise direction. This observation is consistent in all the 24 cases studied. It is for this reason that in this paper we concentrate on the observations in the midspan location, unless it is stated otherwise, which reasonably approximates the separation behavior along the entire cylinder span.

A. Flapping motion of the separated shear layers

Figure 3 shows the instantaneous spanwise vorticity ($\omega_z D_i/U_\infty$) contours at midspan for the case shown in Fig. 2 for six continuous time steps at $\Delta t^* = \Delta t U_\infty/D_i = 1$, where the classical turbulent Kármán vortex shedding can be observed. Perhaps a distinctive feature of the shear layer behavior is the stronger up-and-down flapping motion around the PSP compared to a circular cylinder at a similar Re [42,43], which is also reflected by strong oscillation of the shear layer deflection (or shooting) angle. This flapping motion is accompanied by an oscillatory detachment-reattachment and the temporary appearance of a SSP.

As can be seen in Fig. 3(a) at $t^* = 325$ (phase $\phi \approx 0$, arbitrarily defined), the flow separates from the PSP corner on the lower surface, reattaches to the body, and separates once again from the next corner SSP; while on the top surface, the shear layer flaps away from the surface, without an SSP to appear. Approximately half a shedding cycle later, at $t^* + 4$ (e, $\phi \lesssim \pi$), the separation point distribution flips. At $t^* + 2$ (c, $\phi \approx \pi/2$) and $t^* + 5$ (f, $\phi \approx 5\pi/4$), the shear layers are temporarily at a position in between the maximum flapping amplitude, and only one PSP occurs on each side of the cylinder.

The influence of such shear layer flapping motion extends all the way up to the WSP in a synchronous manner. As shown in Fig. 3, the position of the WSP moves around the windward corner, viz. in cases Figs. 3(a)–3(c) it is on the top half of the cylinder while in Figs. 3(d)–3(f) it is
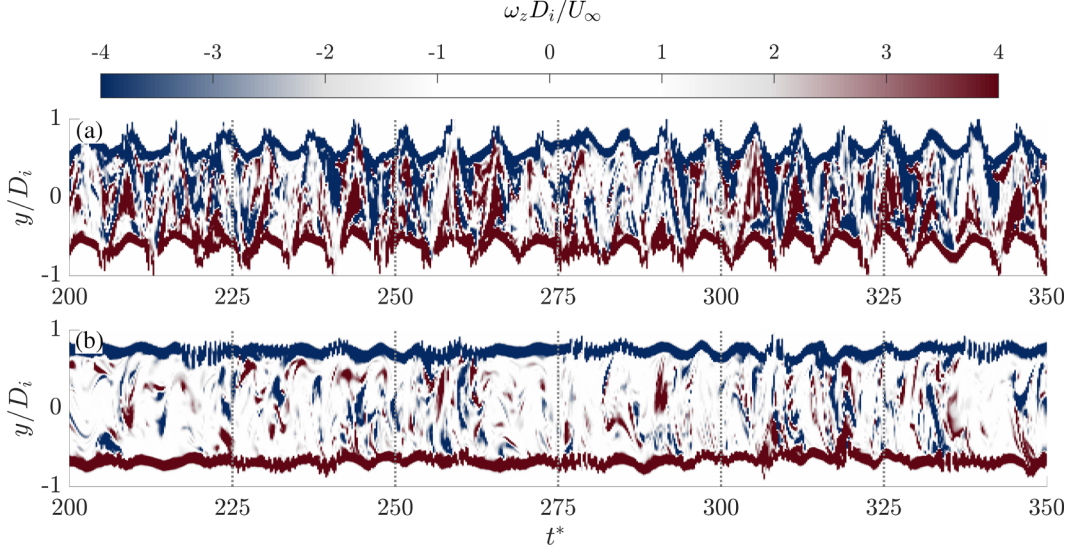
FIG. 4. Space-time contours of the dimensionless spanwise vorticity $\omega_z D_i/U$ at $x = 0.6D_i$ and $-1 \leqslant y/D_i \leqslant 1$ for the case of $N = 7$ at midspan. Here (a) corresponds to $\alpha^* = 0$ and (b) corresponds to $\alpha^* = 0.2$.

on the lower half, even though this is a symmetric case where $\alpha^* = 0$. At face orientation $\alpha^* = 1$, WSP also oscillates around the geometric centreline on the windward surface (figure not shown).

The strength of the flapping motion and the induced synchronous oscillatory motion of the WSP is a universal observation for all the tested cases and is nonlinearly dependent on N and α^*. Not surprisingly, this flapping motion is also in phase with the pressure distribution and therefore the sign of the instantaneous lift coefficient $C_L(t)$, as indicated in Fig. 3. Based on this figure, in cases where the WSP is on the top half of the cylinder, $C_L(t) < 0$ and vice versa. The strength of this flapping motion, however, varies in different cases. Figure 4 shows the space-time contours of the midspan vorticity $\omega_z D_i/U$ for the case of $N = 7$, at $\alpha^* = 0$ and $\alpha^* = 0.2$, respectively. Data is sampled temporally over the range after the wake is fully developed, and spatially over $-1 \leqslant y/D_i \leqslant 1$, and at $x = 0.6D_i$ the streamwise distance before vortices roll up and detach from the shear layer in a time mean sense for both cases [20]. Figure 4 clearly reveals the amplitude of the shear layer flapping motion, being stronger for $\alpha^* = 0$ [Fig. 4(a)] than for $\alpha^* = 0.2$ [Fig. 4(b)].

The strength of this flapping motion behavior of the separated shear layer can be quantified by the spectrum $X(f)$ of the fluctuating streamwise velocity $u'(t)$:

$$X(f) = \int u'(t) \exp(-j2\pi f t) dt. \tag{7}$$

$u'(t)$ is probed at $x = 0.5D_i$ and the y coordinate at the center of the time mean shear layer where the magnitude of the spanwise vorticity ω_z maximizes, which varies for different N and α^*. Thus, the y coordinate is approximately at the mean location of the flapping trajectory for each shear layer at $x = 0.5D_i$. This x coordinate ($x = 0.5D_i$) is chosen for all cases such that $X(f)$ mostly accounts for the shear layer flapping motion strength (in the y direction) without the *direct* influence from the alternative and organized vortex shedding. This will be justified further in Sec. III D.

The result is shown in Fig. 5, together with the dependence of C_D and St on α^* and N. At each α^*, the primary peak of $X(f)$ always occurs at the Strouhal frequency, f_d, which suggests that the behavior of the separated shear layer is primarily associated with the Kármán vortex shedding. The
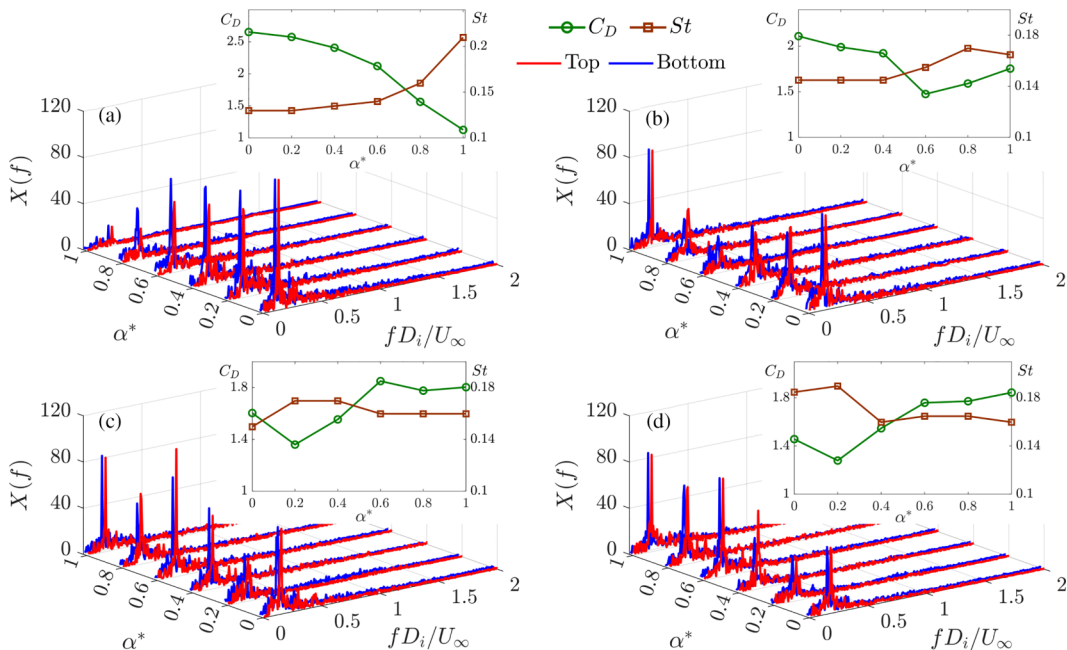
FIG. 5. Shear layer flapping motion strength quantified by the energy spectrum $X(f)$ (arbitrary unit) of fluctuating streamwise velocity component $u'(t)$. Signal is probed at $x = 0.5D_i$ and y coordinate corresponding to the maximum time mean vorticity intensity in the top and bottom shear layers. (a)–(d) are for $N = 5-8$, respectively, in each of which dependence of C_D and St on α^* is also presented.

time mean drag and lift coefficients and Strouhal number are defined as

$$C_D = \frac{F_x}{\frac{1}{2}\rho U_\infty^2 (L_z D_i)}, \quad C_L = \frac{F_y}{\frac{1}{2}\rho U_\infty^2 (L_z D_i)}, \quad \text{St} = \frac{f_d D_i}{U_\infty}, \tag{8}$$

where F_x and F_y are the total time mean drag and lift force, respectively; ρ is the density of the working fluid. f_d is determined from the fluctuating lift coefficient. For convenience purposes, in Eqs. (8) the universal constant D_i is used instead of the more conventional projection width in the streamwise direction, which is an α and N-dependent quantity.

The intensity of the primary peak in the spectra, denoted as $X(f_d)$, is proportional to the strength of the flapping motion, since the characteristic velocity is universal. In particular, we observe that $X(f_d)$ is dramatically low in some cases, e.g., $\alpha^* = 0.6$ for $N = 6$ and $\alpha^* = 1$ for $N = 5$. In these cases, the separated shear layers are relatively stable in the sense that the flapping motion is at very small amplitude compared to the other cases, confirmed by the time history of the instantaneous vorticity fields such as Fig. 3. Results of C_D and St show that for a given N, α^* having the minimum C_D and the maximum St (except $N = 6$) also has the minimum $X(f_d)$. This suggests that the *strength* of the shear layer flapping motion has a direct impact on these two fundamental aerodynamic quantities. Taking a closer examination of $X(f_d)$, we observe in Fig. 5 that $X(f_d)$ behaves nonlinearly with respect to both N and α^*. For $N = 5$ cases, $X(f_d)$ in general inversely depends on α^*, while for $N = 6$, it decreases first until a minimum value is reached at $\alpha^* = 0.6$ before increasing again. $N = 7$ and $N = 8$ cases display a similar variation as $N = 6$, but with the minimum $X(f_d)$ value occurring at $\alpha^* = 0.2$.

Considering the top and bottom shear layers individually, it is clear in Fig. 5 that their spectra both dominate at the Strouhal frequency, notwithstanding the asymmetric distribution of separation point locations, local free stream velocities, and pressure gradients. This asymmetric distribution
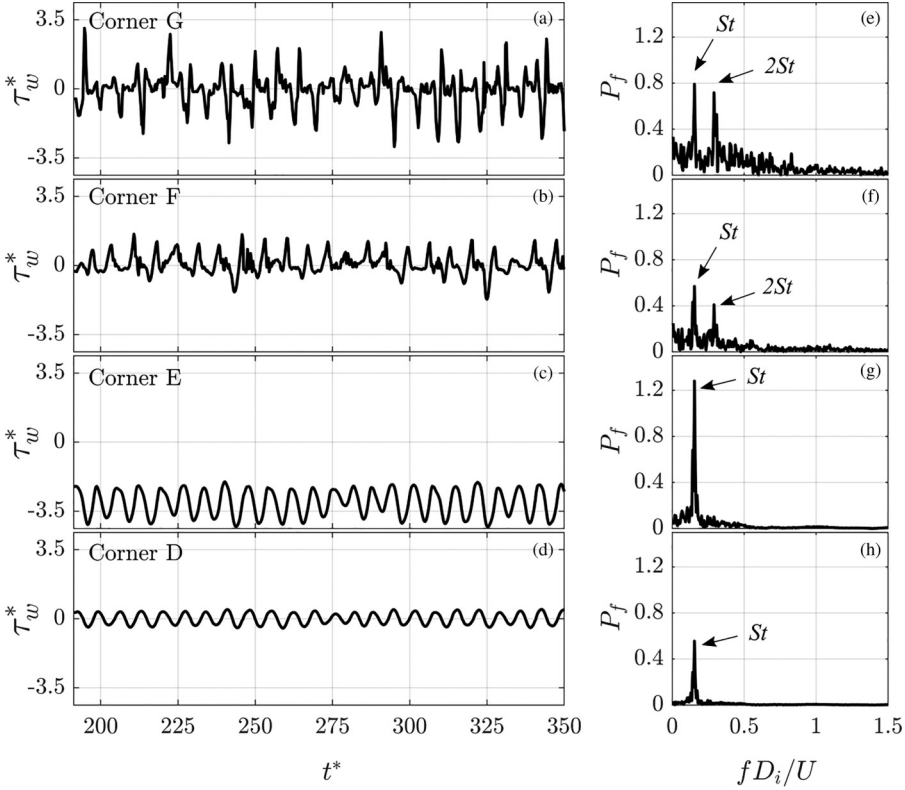
FIG. 6. Normalized midspan instantaneous wall shear stress $\tau_w^*(t)$ on $N = 7$ at $\alpha^* = 0$. For sign convention, see Fig. 7. (a)–(d) are for corners G-F-E-D as marked in Fig. 3(a); (e)–(h) are the corresponding power spectrum density P_f of $\tau_w^*(t)$ in arbitrary units.

is a result of the asymmetric local geometries and separated shear layer deflection angles at off-principal orientations ($0 < \alpha^* < 1$). It is thus unequivocally evident that the global interactive vortex roll-up process in the near wake imposes this synchronization. The intensity of the dominant peak $X(f_d)$, however, is also clearly asymmetric, which reflects the asymmetric *strength* of the separated shear layer flapping motion. Such flapping motion is further affected by the reattachment and the consequent occurrence of the *temporary* SSPs, which will be discussed next.

B. Separation mechanism and separation points

The shear layer separation and reattachment behavior may be well revealed by examining the wall shear stress $\tau_w = \mu(du_\parallel/dy_\perp)$ at $y_\perp = 0$; where μ is the dynamic viscosity, $u_\parallel$ is the flow velocity parallel to the local wall, and $y_\perp$ is the normal distance to the wall. This is calculated by the interior product of the shear stress symmetric tensor and the local polygon surface normal vector. Figure 6 presents the time dependence of normalized wall shear stress $\tau_w^*(t) = \tau_w(t)/\rho f_d^2 D_i^2$ at the corners for the case of $N = 7$, $\alpha^* = 0$, matching the instantaneous vorticity visualization shown in Fig. 3. Owing to the geometrical symmetry of this particular case, the statistical characteristics of $\tau_w^*(t)$ on corners A-B-C are identical to corners G-F-E but with opposite signs.

Evidently, $\tau_w^*(t)$ signals display distinctive features at different corners as shown in Figs. 6(a)–6(d). At corner D, $\tau_w^*(t)$ fluctuates in a sinusoidal manner at a very small amplitude around zero, confirmed by the clear single peak at the Strauhal frequency in its spectrum P_f shown in Fig. 6(h). This is a clear reflection of the oscillation of the windward stagnation point around corner D
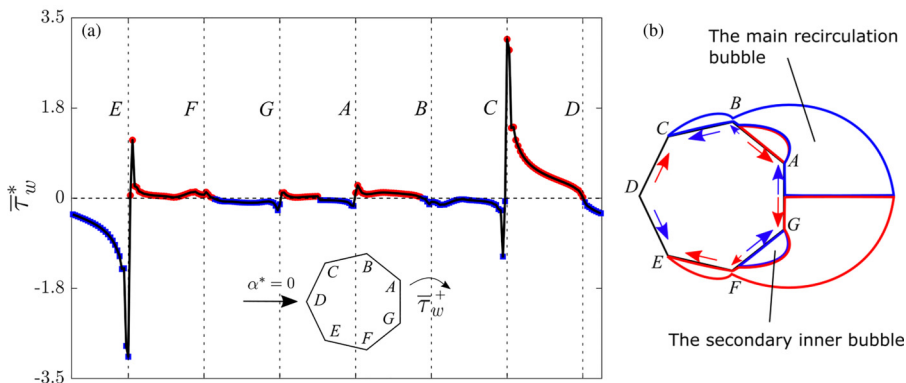
FIG. 7. (a) Distribution of the normalized time mean wall shear stress $\overline{\tau}_w^* = \overline{\tau}_w / \rho f_d^2 D_i^2$ for $N = 7, \alpha^* = 0$. $\overline{\tau}_w$ is considered positive in clockwise direction and is marked by red; negative in counterclockwise direction in blue. (b) Schematic drawing of the recirculation bubble boundaries following the mean streamline pattern. The direction of $\overline{\tau}_w$ on the cylinder surface is marked by arrows; color code follows (a).

highlighted in Fig. 3, supporting the observation that this oscillation stems from the organized vortex shedding in the wake. Corner E in Fig. 6(c) displays a similar neat oscillatory pattern, also supported by the single peak P_f at the Strouhal frequency in Fig. 6(g). However, on the one hand, $\tau_w^*(t)$ is consistently negative, fluctuating around -3.4 instead of zero; on the other hand, the magnitude of P_f is doubled compared to Fig. 6(h), which is a clear manifestation of the shear layer flapping motion, cf. Fig. 5(c). That is, $\tau_w^*(t)$ intensity is strongly influenced by the shear layer deflection angle under oscillatory motion. This is a unique feature for PSP.

The $\tau_w^*(t)$ signals in Fig. 6(a) and Fig. 6(b) exhibit a clear difference to a sinusoidal one, confirmed by the superharmonic peak and the relatively broad band spectra shown in Fig. 6(e) and Fig. 6(f), respectively. Nevertheless, both fluctuate around zero. The ones associated with corner F Fig. 6(b) and Fig. 6(f) are probably related to the temporary reattachment of the separated shear layer. In contrast, corner G shows a similar signal pattern but at higher fluctuating strength. This is due to its location, which is close to the base area and is strongly influenced by the turbulent roll-up of the coherent vortices; see Fig. 3. It is therefore reasonable to postulate that the superharmonics and the relative broad band are a possible result of the combined effect of vortex roll-up and the shear layer flapping motion.

The $\tau_w^*(t)$ signal characteristics at WSP, PSP, (*temporary*) SSP, and the corner in the base region described above can be used to classify any corner in other cases. Furthermore, the fluctuating nature of the signal at any SSP can be used to quantify the fraction of time κ for which the shear layer stays reattached at this point. For the particular example of corner F shown in Fig. 6(b), which is an SSP, reattachment occurs when two conditions are simultaneously considered. That is, $\tau_w^*(t) < 0$ and the phase of the $\tau_w^*(t)$ synchronizes the phase of the corner upstream. This is due to the fact that instantaneously, $\tau_w^* < 0$ can also occur on account of the recirculated flow adjacent to corner F [Fig. 3(e)], instead of shear layer attachment. Calculation of κ is also validated by close examination of the instantaneous vorticity field. It shows that in the fully developed regime, $\kappa \approx 1/4$ for corner F. This is significantly below $1/2$, as one might expect in a simple harmonic flapping motion. The κ value depends on the strength of the flapping motion as well as the exact location of the SSP corner relative to the separated shear layer.

Figure 7(a) presents the distribution of the normalized time mean wall shear stress $\overline{\tau}_w^*$ for the case in Fig. 6, together with the boundaries of the recirculation bubbles around the cylinder surface in Fig. 7(b). First, the strong main recirculation bubbles originating from the PSPs (corners C and E) induce secondary inner bubbles on B-A and F-G; second, due to the relative small time fraction

TABLE I. Reattachment time fraction κ values for SSPs; cf. Fig. 8. Entries marked by $+$ are PSPs, $-$ are not separation points.

	Corner	$\alpha^* = 0$	$\alpha^* = 0.2$	$\alpha^* = 0.4$	$\alpha^* = 0.6$	$\alpha^* = 0.8$	$\alpha^* = 1$
$N = 5$	B	$+$	$+$	$+$	1	1	0.25
	E	$-$	$-$	$-$	$-$	$-$	0.25
$N = 6$	C	$+$	$+$	$+$	$+$	$+$	1
	F	$-$	$-$	$-$	0.02	1	1
$N = 7$	B	0.25	$-$	$-$	$-$	$-$	$-$
	F	0.25	0.08	0.99	1	1	$+$
$N = 8$	C	1	0.35	0.09	$-$	$-$	$-$
	G	1	1	1	$+$	$+$	$+$

of the SSPs, the time mean effect reflects subtle inward deflection of the main recirculation bubble outer boundary at B and F. The complex recirculation bubble shape leaves their footprint clearly on the distribution of $\overline{\tau}_w^*$, which also appears complex.

As expected, at corner D, $\overline{\tau}_w^* = 0$ since the WSP oscillates around it (see Fig. 3). The distribution of $\overline{\tau}_w^*$ is symmetric about the centerline going through corner D; see Fig. 7(b). From corner D to C and D to E, $\overline{\tau}_w^*$ magnitude increases abruptly due to rapid acceleration of the local free stream flow outside the boundary layer, which always is attached; see the thin shear layers on these edges in Fig. 3. Corners C and E experience sharp $\overline{\tau}_w^*$ change, which is a feature of PSPs. Along the edges behind, on C-B and E-F, the magnitude of $\overline{\tau}_w^*$ stays low with the sign changed, owing to the reversed flow inside the main recirculation bubble. The formation of the secondary inner bubbles on edges A-B and G-F causes the sign of $\overline{\tau}_w^*$ to change again. In this particular case, these inner bubbles separate from corner A and G, reattach at about 6° away from B and F, respectively, in time mean sense, reflected by $\overline{\tau}_w^*$ sign change over a very small edge length near B and F. The behavior of $\overline{\tau}_w^*$ in the vicinity of A and G is similar to that at C and E, albeit at much lower intensity and opposite directions. This is because of the similar role these corners played in the local flow. There is a further change of sign for $\overline{\tau}_w^*$ in the middle of A and G, which represents the leeward stagnation point.

Instantaneously, the shear layer flapping motion results in temporary detachment and attachment to corners B and F (Fig. 3), manifesting very different instantaneous recirculation bubble shapes and τ_w^* distribution to the time mean ones shown in Fig. 7. As α^* increases (cylinder rotates clockwisely w.r.t. U_∞), time fraction for the bottom shear layer to stay attached to corner F increases, which eventually becomes fully reattached ($\kappa = 1$) at $\alpha^* \leqslant 0.4$, and then becomes a PSP at $\alpha^* = 1$; while for corner B on the top, κ decreases rapidly from about 1/4 to zero before α^* reaches 0.2. Such κ variation trend is qualitatively consistent for all the other cylinders.

It must be stressed that the κ effect of a SSP originated from the shear layer flapping motion can only be captured and quantified in a time-resolved study, at sufficiently high spatial resolution. If κ is small, *temporary* SSPs can easily be missed in a flow visualisation or a measurement at low speed, i.e., from examining the instantaneous or the time averaged flow field. This explains why the SSP [corner B and F; see Fig. 7(b)] is not captured in the low speed experiments of Xu *et al.* [17] for $N = 7$ corner orientation case but is captured for $N = 5$, $\alpha^* = 1$ and $N = 8$, $\alpha^* = 0$. The observed oscillation of the separation point location on $N = 12$ and 16 cylinders at the principal orientations in their flow visualisation (albeit at transitional Re) is reasonably expected to be related to the flapping motion of the separated shear layer which is discussed here.

The time-averaged PSP and SSP distribution on all the tested cylinders is summarized in Fig. 8, based on the analysis of the mean and the instantaneous wall shear stresses at each corner. The time fraction κ of each SSP is summarized in Table I. It shows that the κ value varies rapidly at the current orientation step $\Delta\alpha^* = 0.2$. For instance, κ increases from 0.01 at $\alpha^* = 0.6$ to 1 (fully
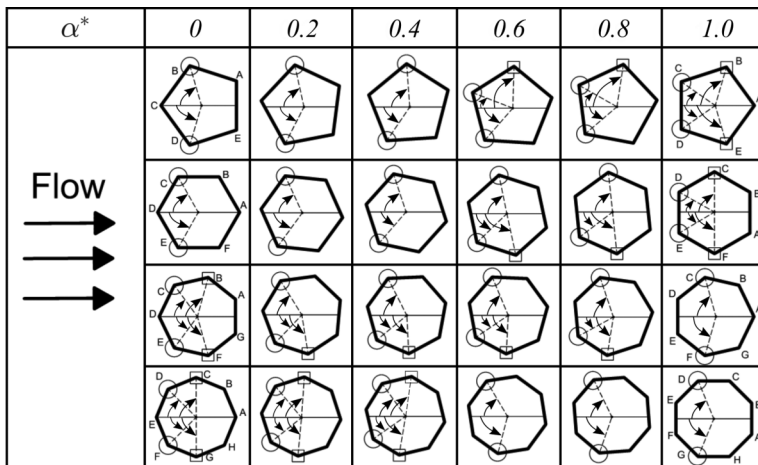
FIG. 8. Time-averaged separation points on polygonal cylinders. Primary separation points (PSPs) are marked by ◯; secondary separation points (SSPs) for attachment time fraction $\kappa > 0$ are marked by □. Curved arrows denote the angle of the separation points θ_s.

reattached) at $\alpha^* = 0.8$ for corner F on $N = 6$. For a given N, the variation of κ on α^* is, in general, monotonic except for $N = 7$ corner F. The lowest κ value at $\alpha^* = 0.2$ is associated with the weakest shear layer flapping motion strength (smallest $X(f_d)$) of $N = 7$; see Fig. 5(c). It may also be noted that the smallest $X(f_d)$ case for each N is also associated with a low κ value.

Figure 8 shows that for all the cases presently studied, separation points always occur on corners (edges) of the cylinder and never on a flat surface. This is consistent with the experimental observations in Xu *et al.* [17]. The SSP, if it appears, is always at the immediate downstream corner of a PSP. This is reassured by $\tau_w^*(t)$ and is also confirmed by the instantaneous vorticity fields $\omega_z(t)$, as well as the mean vorticity fields and the shape of the recirculation bubbles around the cylinders.

The distribution of the PSPs presented in Fig. 8 is plausibly valid for all subcritical Re, since *primary* separation is insensitive to Re in this regime. However, the subtlety of the SSP and the corresponding κ value may not be, as the strength of the shear layer flapping motion could be Re sensitive.

According to Fig. 8 and Table I, dependence of the separation point distribution on α^* can be categorized into two types. As cylinders rotate from $\alpha^* = 0$ clockwisely, the SSP starts to appear on $N = 5, 6$ at $\alpha^* \approx 0.6$, which then remains until the symmetric distribution of PSPs and SSPs at $\alpha^* = 1$. In contrast, for $N = 7$ and 8, cylinders start (at $\alpha^* = 0$) with both PSPs and SSPs, and end (at $\alpha^* = 1$) with PSPs only. The total number of separation points (PSP + SSP) increases with α^* from 2 to 4 for $N = 5, 6$, but decreases from 4 to 2 for $N = 7, 8$. This suggests that there exist two α^*s for each N around which the separation behavior changes appreciably. Comparing with Fig. 5, it could be noted that the total number of separation points is weakly correlated with the general behavior of St and inversely correlated with C_D, which infers the important role separation points played in the general flow characteristics in the near wake. In the next section, their properties will be investigated.

C. Separation angles

To facilitate discussion, we denote T_0 to be the corner on the polygon corresponding to the maximum height and T_1 the corner upstream of T_0; see Fig. 9. The associated angle of the edge $T_0 - T_1$ w.r.t. U_∞, denoted by θ_0, can be calculated analytically, for the top (+) and bottom surfaces
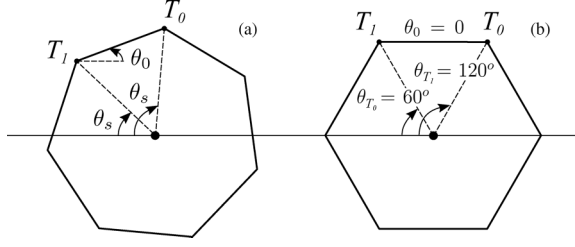
FIG. 9. Definition of T_0, T_1 and θ_0 for (a) an arbitrary incidence angle where T_0 is unambiguous and (b) case $N = 6$, $\alpha^* = 0$ where T_1 and T_0 have the same height. The other case is $N = 8$, $\alpha^* = 1$ (not shown here). All the angles are measured from the horizontal axis, viz. the incoming flow direction.

$(-)$, respectively, as

$$\theta_0^{(\circ)} = \pm\gamma\left(\frac{180}{N}\right) + \begin{cases} 0 & 0 \leqslant \gamma < 2 \\ 360/N & \text{otherwise,} \end{cases} \tag{9}$$

where

$$-\gamma = \pm\alpha^* - \begin{cases} 0 & N = 4n - 2 \\ 0.5 & N = 4n - 1 \\ 1 & N = 4n \\ 1.5 & N = 4n + 1, \end{cases} \tag{10}$$

in which n is an arbitrary integer. γ is categorized into four conditions because of the observed periodic behavior of θ_0 in every four counts of N. After θ_0 is found, the separation angle θ_s, viz. the angular position of corner T_0 and T_1 (see Fig. 9), can be determined analytically as

$$\theta_s^{(\circ)} = (\alpha^* \pm 2p)\left(\frac{180}{N}\right) - \begin{cases} 0 & 0 \leqslant \gamma < 2 \\ 360/N & \text{otherwise,} \end{cases} \tag{11}$$

where $(+)$ and $(-)$ are for the top and bottom surfaces, respectively. $p = \lceil(N - 1)/4\rceil$ for T_0 and $p = \lceil(N - 1)/4\rceil - 1$ for T_1. The ceiling function $\lceil\cdot\rceil$ denotes the nearest larger integer. This is similar to Eq. (1). In the present paper, we use degree to quantify θ_0 and θ_s and radian for the shear layer deflection angle to be discussed in Sec. III D.

Equations (9)–(11) are plausibly valid for $2 \leqslant N \ll \infty$. For the asymptotic circular cylinder case $(N \to \infty)$, θ_0 is supposed to be the angle of the tangent line at the separation point, which is $\approx 12°$ according to the flow visualization in Xu et al. [17], while $\alpha^* = 0$ yields $\theta_0 = 0°$ from Eq. (9) and $\theta_s = \pm90°$ from Eq. (11). Note that in the absence of the transition at the present Re, θ_0 is equivalent to ξ in Eq. (1), which is a robust scaling parameter for C_D and St, also accounting for the transition effect. However, unlike ξ, θ_0 is asymmetric at an off-principal α.

Utilizing the denotations in Fig. 9, similar for the bottom half of the cylinder, three scenarios could be identified in Fig. 8:

(i) Flow only separates from T_0.

(ii) Flow only separates from T_1.

(iii) Flow separates from T_1, but reattaches to the cylinder and then separates again from T_0. Shear layer flapping motion further categorizes it, based on κ values in Table I, as $\kappa = 1$ and $0 < \kappa < 1$.

From θ_0 calculated in Eq. (9), we can empirically predict the occurrence of each scenario, hence the separation angle θ_s of each separation corner with Eq. (11), also for intermediate incidence

TABLE II. Evaluation of separation angles based on Eqs. (11) and (12) for $N = 5$ cases. †, ‡ indicate the angles where switch of separation from T_0 to T_1 occurs following the arrows.

♯ θ (deg)	$\alpha^* = 0$	$\alpha^* = 0.2$	$\alpha^* = 0.4$	$\alpha^* = 0.6$	$\alpha^* = 0.8$	$\alpha^* = 1.0$
1 $\theta_0(T)$	54	46.8	39.6	32.4	25.2	18
2 $\theta_0(B)$	-54	-61.2	-68.4	-3.6	-10.8	-18
3 $\theta_s(T_0^T)$	72	79.2	†86.4	93.6	100.8	108
4 $\theta_s(T_0^B)$	-72	-64.8	‡-57.6	-122.4	-115.2	-108
5 $\theta_s(T_1^T)$	0	7.2	14.4	21.6	28.8	36
6 $\theta_s(T_1^B)$	0	-7.2	-14.4	-50.4	-43.2	-36
7 $\theta_s(\text{PSP}^T)$	72	79.2	†86.4	21.6	28.8	36
8 $\theta_s(\text{PSP}^B)$	-72	-64.8	‡-57.6	-50.4	-43.2	-36
9 $\theta_s(\text{SSP}^T)$	-	-	-	93.6	100.8	108
10 $\theta_s(\text{SSP}^B)$	-	-	-	-	-	-108

angles which are not presently studied, as

$$\theta_s = \begin{cases} \theta_s(T_0) \text{ only} & \left|\theta_0^{(\circ)}\right| \geqslant 36 \quad \text{(i)} \\ \theta_s(T_1) \text{ only} & \left|\theta_0^{(\circ)}\right| \leqslant 12 \quad \text{(ii)} \\ \theta_s(T_1) \; \rightarrow \; \theta_s(T_0) & 12 < \left|\theta_0^{(\circ)}\right| < 36 \quad \text{(iii)}. \end{cases} \tag{12}$$

The thresholds $\theta_0 = 12°$ and $36°$ are associated with the case $N = 6$, $\alpha^* = 0.4$ corner E, and $\alpha^* = 0.8$ corner C, respectively; see Fig. 8.

Taking $N = 5$ cases as an example, Table II summarizes how Eqs. (9)–(12) predict the separation behavior and the corresponding separation angles. Starting from N and α^* values, θ_0 for top and bottom surfaces can be calculated from Eq. (9) (rows 1 and 2). The condition in Eq. (12) predicts where the flow will separate (T_1 and/or T_0) and the exact location (θ_s) is calculated in Eq. (11) (rows 3–6). The corner characteristics are presented in the last four rows; see also Figs. 8 and 10, which also mark the θ_0 values tabulated in rows 1 and 2.

For $0 \leqslant \alpha^* \leqslant 0.4$, flow separates from T_0 (as PSPs) symmetrically (rows 7 and 8; see also Fig. 10). Within $0.4 < \alpha^* < 0.6$, the PSP switches to T_1 on the top surface. The top T_0 becomes a SSP for $\alpha^* \geqslant 0.6$ (row 9) while reattachment does not occur on the bottom surface until $\alpha^* = 1$ when T_0 becomes a SSP symmetrically (row 10). This switch is indicated by the arrows.

θ_s calculated from Eqs. (11) and (12) are shown in Fig. 11. Cases included are $3 \leqslant N \leqslant 20$. It has been shown in Xu *et al.* [17] that at Re $= 10^4$, cylinders of $N \leqslant 16$ do not undergo transition, at least in their principal orientations, and the critical Re where the transition occurs increases with N. It thus is reasonable to expect that this pattern is valid for a polygonal cylinder having arbitrary N at subcritical Re, where the PSP is fixed at a predictable corner.

A pattern emerges if the data points at the same α^* are connected. For a given N, shear layer reattachment and the occurrence of the SSP is reflected by two markers at the same α^*, one for T_0 and the other for T_1. From this pattern, one could possibly predict with reasonable accuracy the primary separation and also the reattachment behavior for polygons of not too large N at arbitrary α. Reattachment behavior, hence the occurrence of the SSP, is less certain because of the unknown flapping motion strength at large N. However, it successfully predicts $N = 16$ at $\alpha^* = 0, 1$ verified by experiment. For the case of $N = 12$, PSPs at the two principal orientations are captured, but the SSP at $\alpha^* = 0$ is not reported in the experiment. This is likely owing to the experiment of Xu *et al.* [17] being done in a low-speed manner, where reattachment was missed as mentioned above. In particular, $\theta_0 = 15°$ in this case, calculated from Eqs. (9) and (10). This is very close to $\theta_0 = 18°$ in
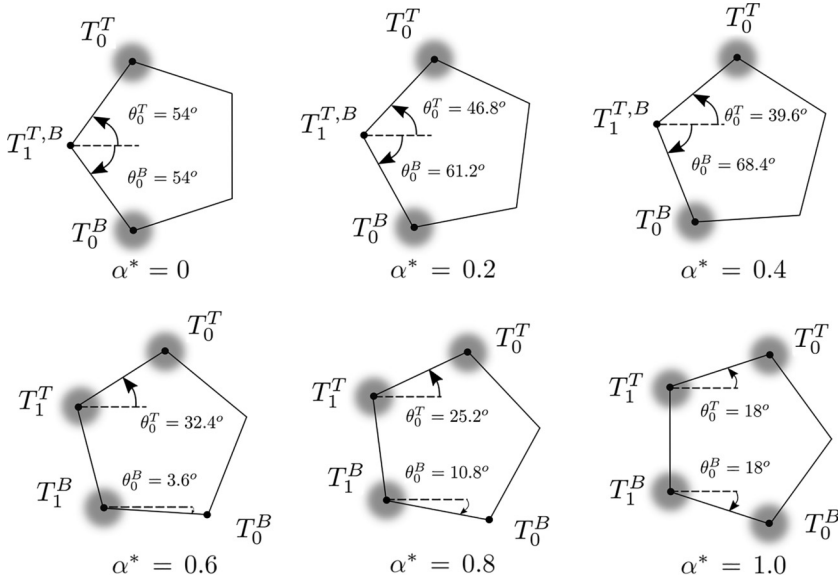
FIG. 10. Switch of corner characteristics for $N = 5$ cases.

$N = 5, \alpha^* = 1$; see Fig. 10. According to Table I, the former case is likely to have $\kappa < 0.25$, which is a small fraction of reattachment time.

The data points are clearly clustered in two regions enveloped, subjected to uncertainty from the present resolution $\Delta \alpha^* = 0.2$. Notwithstanding the asymmetric pattern of data points about $\theta_s = 0$
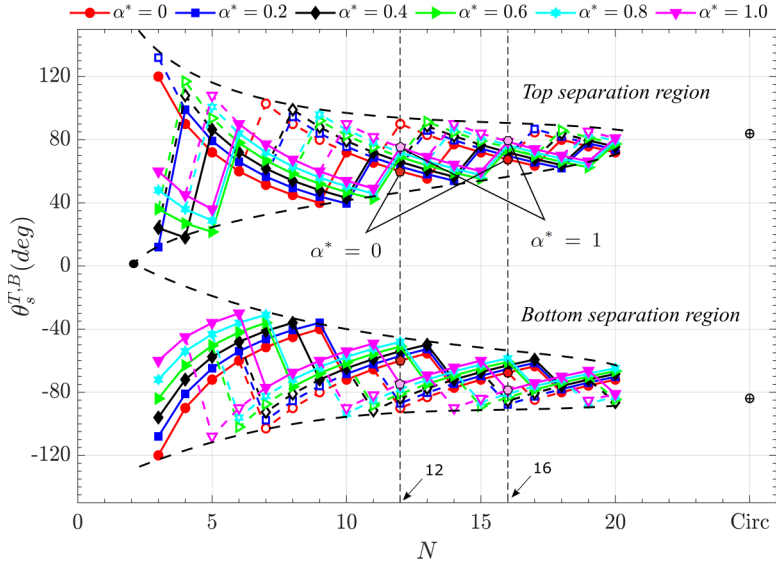

FIG. 11. The pattern of the separation angles $\theta_s^{T,B}$ and the associated envelope curves for the separated region at Re $= 10^4$. The θ_s values are calculated by Eqs. (11) and (12); filled markers are for PSPs and open markers for SSPs. Data points for $N = 12, 16$ for corner and face orientations are taken from Xu *et al.* [17], which are PSPs symmetrically distributed about the $\theta_s = 0$ axis. Data points for the circular cylinder are taken from Jiang [44]. Dashed curves approximate the envelopes of the data points.
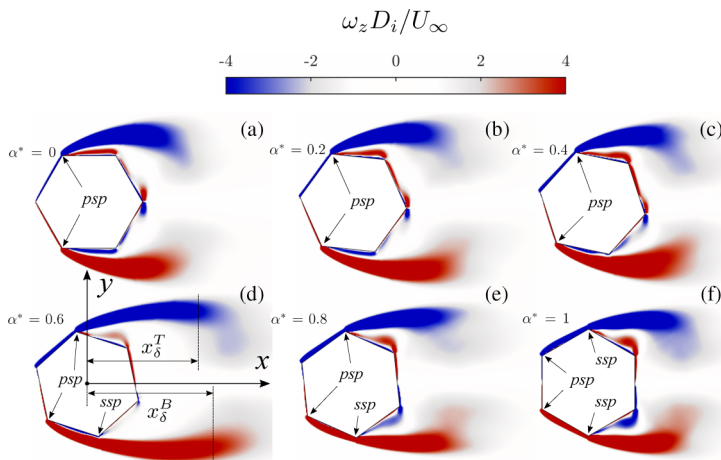
FIG. 12. Time mean and spanwise averaged ω_z for the hexagonal cylinder. $x_\delta^{T,B}$ is the characteristic shear layer penetration distance.

(complete symmetry follows $-\alpha^*$ cases), the envelopes appear symmetric. The enveloped regions are separation angles, including PSPs and SSPs, that most likely will occur for a polygonal cylinder of arbitrary N at Re $= 10^4$ or a subcritical Re. As might be expected, the θ_s range covered by the envelope boundaries diminishes as N increases and eventually converged to the circular cylinder case at the far end. The inner boundaries of the two regions collapse at $N = 2$, $\theta_s = 0$, i.e., the flat plate at the streamwise (or corner) orientation which is well predicted.

D. Signature in the time mean separated shear layer

The instantaneous shear layer flapping motion leaves a clear signature in the mean vorticity field and leads to interesting consequences. The mean field is time and spanwise averaged. Figure 12 shows the ω_z contours for the hexagonal cylinder at all α^*. The ω_z contours for all cases studied can be found in Masoudi *et al.* [20]. They reveal that the penetration distance of the shear layer into the wake in the streamwise direction, as well as their thickness, vary with α^* in a nonlinear way. It can also be noted that, in general, these two quantities are inversely correlated. That is, a thinner shear layer tends to penetrate further downstream. At $\alpha^* = 0.6$, it penetrates the furthest. This is a universal observation for all other cylinders (figure not shown). Since every phase of the instantaneous shear layer flapping motion contributes to the time mean, it suggests that when the flapping motion is less strong, the shear layer is more stable, leading to a further vortex roll-up distance, viz. a larger formation length [20].

Figure 13 presents the development of the mean shear layer thickness $\delta^{T,B}$ based on a properly chosen threshold $\omega_z D_i/U = 3$, where the penetration distances for the top (T) and bottom (B) shear layers are examined separately. As can be seen, $\delta^{T,B} > 0$ at $x = 0$, which indicates that the PSPs of all tested cases are at $x < 0$. For a number of cases, the SSP occurs within $0 < x \lesssim 0.2D_i$ (the maximum value $0.2D_i$ being for $N = 5$, $\alpha^* = 1$; see Fig. 8), where $\delta^{T,B}$ over this range measures the thickness of either the separated boundary layer before reattachment or the reattached boundary layer. This implies that at $x = 0.5D_i$, the characteristic base point location, shear layers in all cases are finally separated with no further reattachment. At the same time, Fig. 13 shows that $d\delta/dx > 0$ at $x = 0.5D_i$, where shear layer is developing before vortex shedding in a statistical sense. It thus reassures that the flapping motion strength measured by $X(f)$ at $x = 0.5D_i$, presented in Fig. 5, largely excludes the effect of coherent vortex roll-up.

Figure 13 shows that $\delta^{T,B}$ increases rather smoothly until the maximum value, denoted as $\delta^{T,B}_{\max}$, is reached with a similar pattern through all the cases. For small x within the range of $d\delta/dx > 0$,
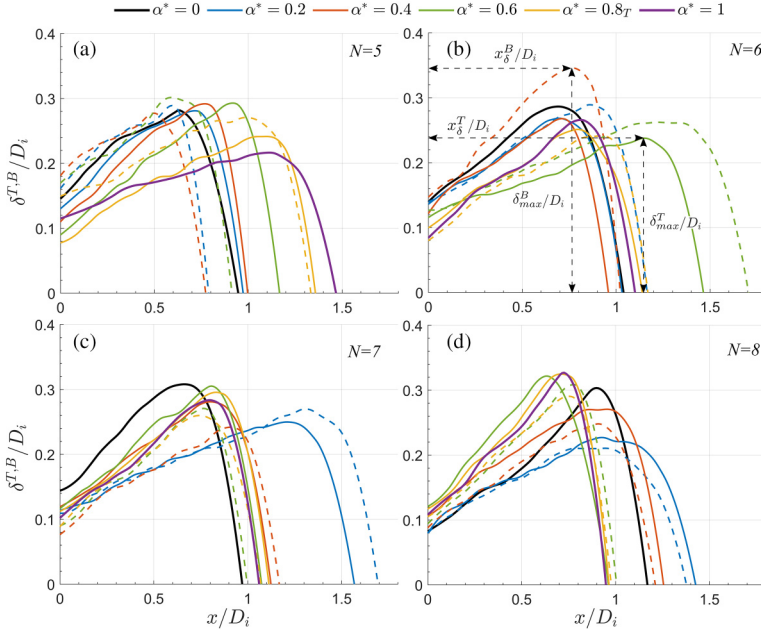
FIG. 13. Streamwise development of the mean shear layer thickness $\delta^{T,B}$ based on vorticity threshold $\omega_z D_i/U = 3$; Solid lines are for the top and dashed lines for the bottom.

as N increases, dependence of $\delta^{T,B}$ on α^* is appreciably weaker. Weak waviness of $\delta^{T,B}$ can also be observed in this range in some cases, e.g., the top shear layer of $N = 5$, $\alpha^* = 0.6$ at $x \approx 0.4D_i$, in between the PSP and SSP (cf. Fig. 10). This is the footprint of the separation bubble between the separated shear layer and the surface of the cylinder directly underneath. The distance at which $\delta^{T,B}_{\max}$ occurs is denoted as $x_\delta^{T,B}$. Downstream of $x_\delta^{T,B}$, the thickness $\delta^{T,B}$ drops in steep slopes, indicating that $x_\delta^{T,B}$ is the time mean location where the rolled-up vortices start to detach from the separated shear layer. This characteristic distance for $N = 6$, $\alpha^* = 0.6$ is marked in Fig. 12.

It is also evident in Fig. 13 that at off-principal orientations, for a given α^* the asymmetric geometry about the flow direction results in asymmetric shear layer thickness $\delta^{T,B}$, its growth rate $d\delta/dx$, and the corresponding penetration distance $x_\delta^{T,B}$. The variation of $x_\delta^{T,B}$ is presented in Fig. 14(a), which shows that the dependence of x_δ^T and x_δ^B on α^* for a given N is consistent, under the effect of mutual interaction between the top and bottom shear layers. It can also be observed in this figure that in principal orientations, the variations of $x_\delta^{T,B}$ on N are opposite at $\alpha^* = 0$ and 1 [dotted lines in Fig. 14(a)].

In most cases and for both top and bottom surfaces, the shear layer is thicker when the PSP locates further upstream. In cases having SSPs, particularly temporary SSPs, the shear layer appears thinner as a result of reattachment. This also is a reflection of the flapping motion amplitude, as stronger flapping leaves a thicker time mean footprint.

As might also be expected, as N increases, $\delta^{T,B}$ becomes less α^* dependent, since the data range becomes appreciably smaller in the $d\delta/dx > 0$ range. For $N \to \infty$ (the circular cylinder), δ would lose the α effect and be symmetric for the top and bottom.

For a given N, there appears to be a particular α^* where shear layers penetrate substantially further downstream than other α^*, e.g., $\alpha^* = 0.6$ for $N = 6$ and $\alpha^* = 0.2$ for $N = 7$, as illustrated in Fig. 14(a). The distance of the furthest penetration, as well as α^* at which it occurs, behave nonlinearly upon N. The mean shear layer penetration distance can also be quantified by a chosen vorticity threshold ($\omega_z D_i/U = 3$) and is denoted as L_ω [20]. Figure 14(b) demonstrates their
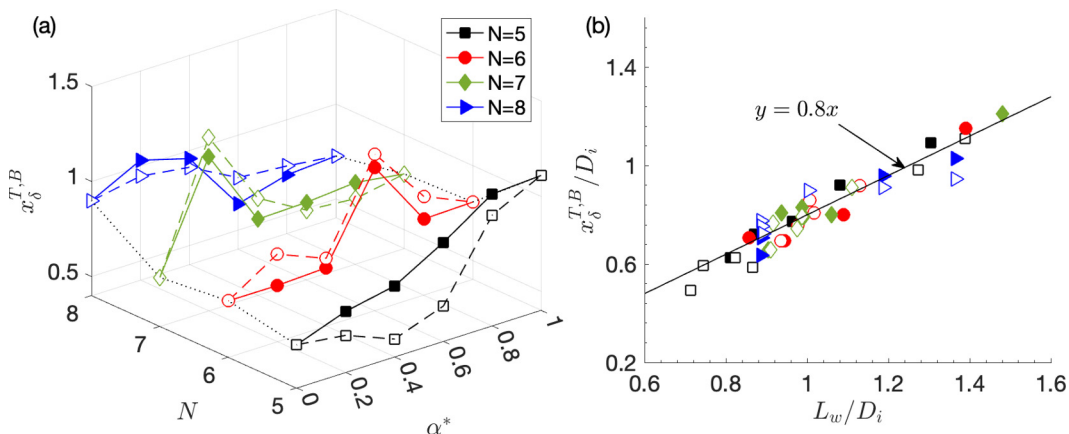
FIG. 14. (a) Shear layer penetration distance x_δ^T and x_δ^B, (b) correlation of $x_\delta^{T,B}$ and shear layer penetration distance L_w based on vorticity threshold $\omega_z D_i/U = 3$. The solid markers are for the top shear layer and the open markers for the bottom.

correlation. The degree of correlation is insensitive to the vorticity threshold value, but the slope has a weak dependence. However, it is evident that the two lengths are well correlated. These two length scales are also linearly proportional to the vortex formation length L_f, determined by the x coordinate of the maximum turbulent kinetic energy; figure not shown.

Masoudi *et al.* [20] found that L_ω is a proper parameter which scales negatively with C_D and the wake displacement thickness D_w calculated at $x = L_f$, and positively with St and the mean base pressure coefficient C_p. The scaling quality is not sensitive to the chosen vorticity threshold value, even though the absolute value of L_ω is. The correlation in Fig. 14(b) assures that $x_\delta^{T,B}$ is also a proper length scale in this sense, which is less dependent on a chosen threshold value. This is confirmed in Fig. 15(a) with reasonable data collapsing, which shows that a longer shear layer penetration distance leads to a higher vortex shedding frequency and an appreciable smaller drag. This also verifies the inverse relation between C_D and St (Fig. 5), as commonly observed in general cylindrical-shaped bluff bodies [17,21–23].

The inverse correlation of C_D with $x_\delta^{T,B}$, a length scale in the streamwise direction, is also supported by its positive correlation with the weakly varying wake width D_w, which asymptotically approaches D_i at large $x_\delta^{T,B}$, as shown in Fig. 15(b). At $x = L_f$, where D_w is calculated, the pressure variation along the y direction is significant, which results in a weak correlation of C_D and the momentum wake width there; figure not shown.

In line with Bearman [45] for their bluff body in a similar Re, Fig. 15(c) confirms the linear relation between the product StC_D and $\sqrt{1 - (C_p)_b}$, where $(C_p)_b$ here takes the averaged pressure coefficient value over the base area, viz. the surface between the top and bottom PSP. $(C_p)_b$ is found to be fairly constant over this area [20].

Quantifying the strength of the flapping motion by the energy content of the spectrum peak $X(f_d)$ in Fig. 5 as

$$\Lambda = \frac{1}{U_\infty} \int_{f_d - \Delta f}^{f_d + \Delta f} X(f_d) df, \tag{13}$$

where $\Delta f D_i/U_\infty = 0.02$. Figure 16 suggests that stronger flapping motion induces a destabilizing effect to the separated shear layer and results in a shorter penetration distance. Referring to Fig. 15(a), this also corresponds to a lower vortex shedding frequency (smaller St).
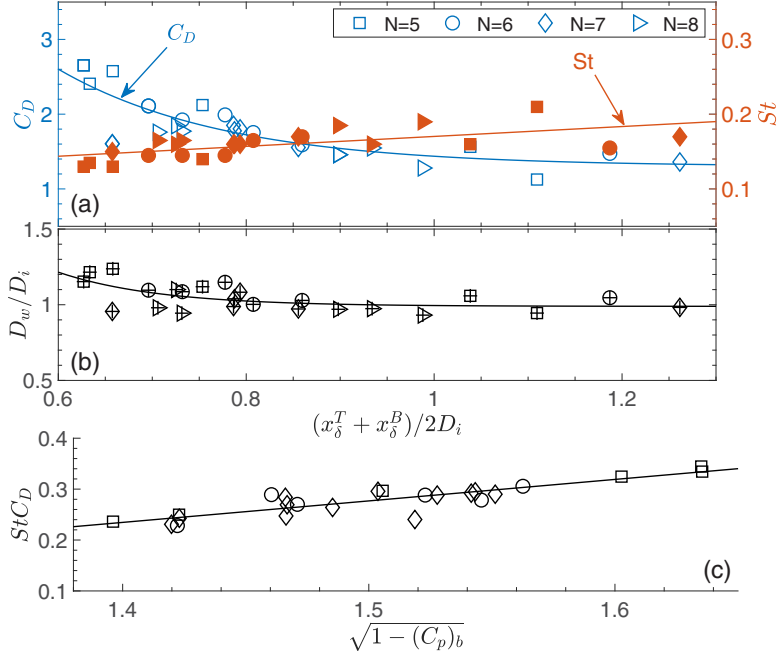
FIG. 15. Dependence on the averaged shear layer penetration distance $(x_\delta^T + x_\delta^B)/2$ of (a) C_D and St, (b) the wake displacement thickness D_w measured at the formation length. Solid lines are arbitrary fitting curves. (c) Correlation of StC_D and $\sqrt{1 - (C_p)_b}$.

Since the shear layer thickness δ grows almost linearly on x before $\delta_{max}^{T,B}$ is reached, as shown in Fig. 13, we could approximate the growth rate as

$$\frac{d\delta}{dx} \approx \frac{\delta_{max}^{T,B} - \delta^{T,B}|_{x=0}}{x_\delta^{T,B}}, \tag{14}$$

which is insensitive to the vorticity threshold value for δ calculation. Figure 16 also suggests that the flapping motion strength is proportional to the *time mean* shear layer thickness growth rate, which is plausibly attributed to three effects: the absolute the shear layer intensity at the separation point
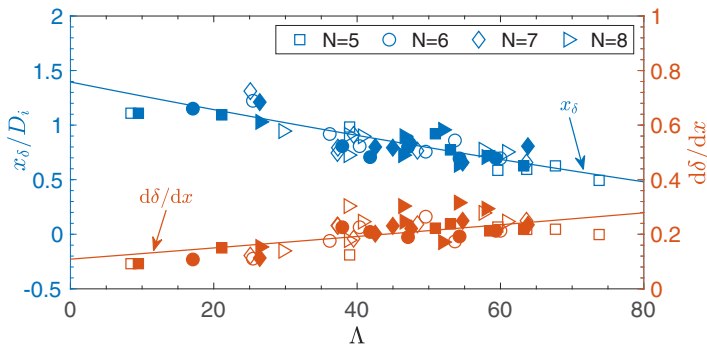

FIG. 16. Dependence on the shear layer flapping motion strength Λ of the shear layer penetration distance $x_\delta^{T,B}$ and the shear layer thickness growth rate $d\delta/dx$. Open and solid markers are for the top and the bottom shear layer, respectively. Solid lines are arbitrary fitting curves.
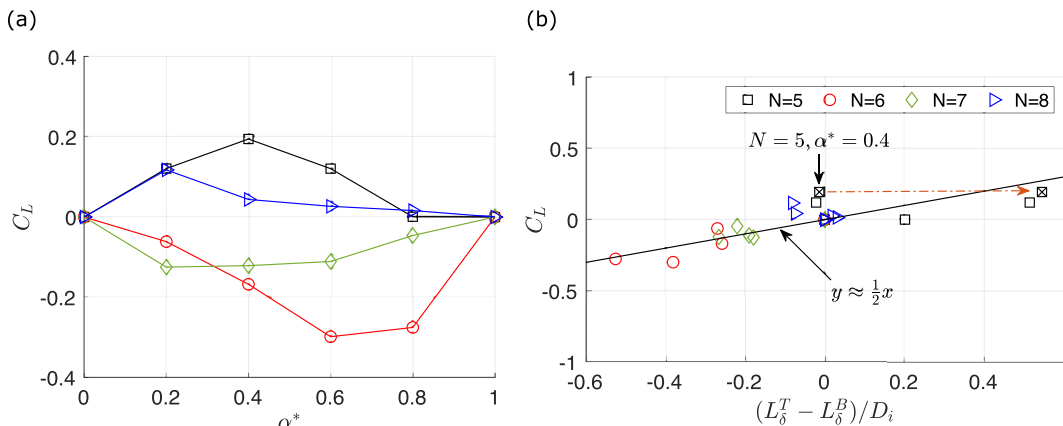
(a)

(b)

FIG. 17. (a) Dependence of (the time mean) C_L on α^*. (b) Dependence of C_L on the difference of the top and bottom shear layer lengths $L_\delta^T - L_\delta^B$.

and the vorticity diffusion effect; the strength of the recirculated flow between the separated shear layer and the cylinder surface, as well as the possible reattachment to SSP; and the strength of the flapping motion. One could possibly speculate from Fig. 3 that the instantaneous $d\delta/dx$ does not depend strongly on the first effect, and therefore the variation of the mean growth rate is flapping motion driven but affected by reattachment. The degree of correlation in Fig. 16 is not sensitive to the chosen Δf for Λ calculation, as long as it focuses reasonably around f_d.

According to Kelvin's circulation theorem, the asymmetric penetration distance $x_\delta^{T,B}$ at off-principal orientations suggests that cylinders experience nonzero time mean lift. Indeed, this is confirmed in Fig. 17(a). Moreover, even though all cylinders rotate clockwisely from corner orientation ($\alpha^* = 0$) to face orientation ($\alpha^* = 1$), the sign and magnitude of C_L vary nonlinearly w.r.t. N. For instance, $C_L > 0$ for $N = 5, 8$ but $C_L < 0$ for $N = 6, 7$. Denoting the shear layer length to be $L_\delta^{T,B}$, which is the distance between $x_\delta^{T,B}$ and the corresponding PSP, circulation associated with each separated shear layer $\Gamma_S^{T,B}$ scales with it. The contribution from the attached boundary layer is neglected, which is a fair assumption according to the flow visualization in Fig. 3.

Figure 17(b) shows that $C_L \sim (L_\delta^T - L_\delta^B)/2D_i$, reasonably correlated for both sign and magnitude, regardless of N and α^*. Considering instantaneous vortex shedding behavior (Fig. 3), this suggests that comparing to the length difference, the instantaneous shear layer strength does not vary significantly with α or N. For the case of $N = 5, \alpha^* = 0.4$, θ_0^T ($= 39.6°$, see Fig. 10) is close to the threshold $36°$ in Eq. (12), where the boundary layer on the surface upstream the top PSP is just about to separate (in the time mean sense). Therefore, it appears thicker than well-attached boundary layers in other cases; figure not shown. If this thick boundary layer is taken into account, the shifted marker would reflect a better collapse onto the fitted line. Distribution of the markers in Fig. 17 also suggests that the shear length difference $|L_\delta^T - L_\delta^B|$ diminishes as N increases, until it completely vanishes with angle of attack effect and hence the time mean $C_L \to 0$ for the circular cylinder case ($N \to \infty$).

The above discussions suggest that the shear layer penetration distance in the streamwise direction, associated with the averaged vortex shedding distance and the shear layer flapping motion strength, is a reasonable length scale for C_D, C_L, and St. Considering that C_D and St also scale with the characteristic wake width in the transverse direction [17,46,47] (see also Fig. 15), we propose the deflection angle β_w of the mean separated shear layer to be an effective scaling parameter, which takes into account the length scales in both streamwise and transverse directions. Denoting the y coordinate of the maximum ω_z magnitude in the two shear layers along $x = x_\delta^{T,B}$ (see Fig. 13) to be
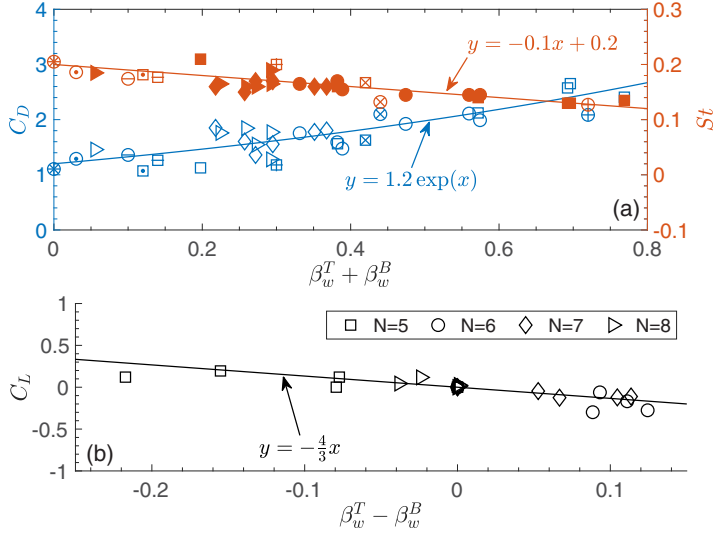
FIG. 18. (a) Dependence of C_D and St on the deflection angle between the top and bottom shear layers $\beta_w^T + \beta_w^B$; also shown are data from the experiments of Xu *et al.* [17] and Wang *et al.* [18] at a similar Re, where $\circledast$ is for the circular cylinder; markers $+$, $\times$, $-$, $\bullet$ are for $N = 3, 4, 12, 16$, respectively, which are wrapped by $\square$ and $\circ$ for $\alpha^* = 0$ and 1 (principal orientations). (b) Dependence of C_L on the deflection angle asymmetry $\beta_w^T - \beta_w^B$.

$y_\delta^{T,B}$, we may approximate this deflection angle to be

$$\beta_w^{T,B} = \tan^{-1}\left(\frac{\left|y_\delta^{T,B}\right| - R_i}{x_\delta^{T,B}}\right). \tag{15}$$

The absolute value of $y_\delta^{T,B}$ is used to characterize the magnitude of the deflection angle without the sign effect. In all cases studied, $|y_\delta^{T,B}|$ is always larger than the in-circle radius R_i. Although, in reality, shear layer separates from a corner (an edge) associated with the circum-circle radius R_c, here R_i is used instead, since it is a universal constant independent of N and α^*. Figure 18 shows that $\beta_w^{T,B}$ results in noticeably better scaling compared to $x_\delta^{T,B}$ (cf. Fig. 15 and 17). The total deflection angle between the top and bottom separated shear layers $\beta_w^T + \beta_w^B$ is proportional to C_D and inversely proportional to St, while their difference $\beta_w^T - \beta_w^B$ scales inversely with C_L, which is in line with a standard control volume analysis. It is also consistent with the averaged base pressure coefficient C_p [20] that a larger deflection angle results in a lower $(C_p)_b$ associated with a shorter shear layer penetration distance and a wider low pressure base area (figure not shown), hence larger C_D. Figure 18(a) also includes $N = 3, 4, 12, 16$ cases with C_D and St values taken from Xu *et al.* [17] and $\beta_w^{T,B}$ from Wang *et al.* [18]. For $N = 3$ and $N = 4$, $\alpha^* = 0$ cases, C_D and St are calculated based on the projected width of the cylinder instead of D_i [see Eq. (8)]; values for $N = 12, 16, \alpha^* = 0$ cases are converted to be based on D_i.

All the correlations can be empirically described by relatively simple functions, i.e.,

$$C_D \approx 1.2\exp\left(\beta_w^T + \beta_w^B\right), \tag{16}$$

$$C_L \approx -\tfrac{4}{3}\left(\beta_w^T - \beta_w^B\right), \tag{17}$$
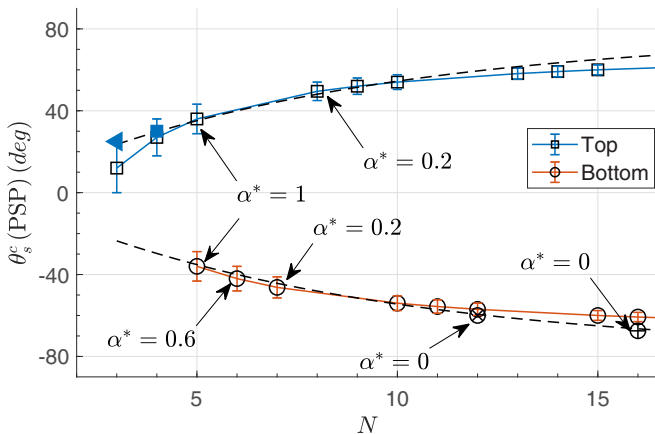
$$St \approx -0.1\left(\beta_w^T + \beta_w^B\right) + 0.2. \tag{18}$$

FIG. 19. Critical PSP angles on top and bottom surfaces. Also shown are ▲ for $N = 3$ from Huang $et\ al.$ [8] ■ for $N = 4$ from Iungo and Buresti [7], $\otimes$ for $N = 12$, $\alpha^* = 0$, and $\oplus$ for $N = 16$, $\alpha^* = 0$ taken from Xu $et\ al.$ [17]. Solid lines and open markers with error bars are for Eq. (20) and dashed lines Eq. (21).

In particular, the fitting constant 0.2 in Eq. (18) corresponds to St of a circular cylinder at Re $= 10^4$. This suggests that $\beta_w^T = \beta_w^B \approx 0$ for a circular cylinder, which also results in $C_D \approx 1.2$ and $C_L = 0$ in Eqs. (16) and (17), respectively [18].

It can also be noted from Fig. 18(a) that the range between the largest ($N = 5$, $\alpha^* = 0.4$) and smallest (the circular cylinder) total deflection angle $\beta_w^T + \beta_w^B$ is significant. In general, as N increases, it decreases, e.g., for $N \rightarrow \infty$ (circular cylinder), $\beta_w^T + \beta_w^B \approx 0$. In Eq. (15), $\beta_w^{T,B}$ may also be approximated by the true shear layer maximum deflection distance $y_{\max}^{T,B}$, viz. the maximum y coordinate of the mean shear layer centroid trajectory, and the associated x coordinate $x_{\max}^{T,B}$. The resultant scaling quality is similar but slightly lower, as it is found that $y_\delta^{T,B} \approx y_{\max}^{T,B}$, $x_\delta^{T,B} \approx (5/4) x_{\max}^{T,B}$, which suggests that shear layers have very small curvature.

E. Critical separation angle

It is evident from Fig. 14(a) that both the top and bottom shear layer penetration distance x_δ maximize at $\alpha^* = 1, 0.6, 0.2$, and 0.2, respectively, for $N = 5 \sim 8$. From Figs. 15 and 18, it can be concluded that this α^* corresponds to maximum St and minimum C_D, $\beta_w^T + \beta_w^B$, and Λ. Except for $N = 5$, in other polygons α^* occurs at off-principal orientation, and therefore $x_\delta^{T,B}$ is asymmetric. It is found that the side (top or bottom) with a larger x_δ in these cases is associated with $|\theta_0| \approx 18°$ (refer to Fig. 9). It is the top side for $N = 8$ ($\theta_0 \approx 18°$) and the bottom side for $N = 6, 7$ ($\theta_0 \approx -18°$); for $N = 5$, it is symmetric $\theta_0^T = \theta_0^B = 18°$ (Fig. 10, $\alpha^* = 1.0$). For the square cylinder, $\theta_0 = 15°$ [8,48]. We therefore propose an empirical equation that associates the largest shear layer penetration distance (on a single side) with θ_0 by

$$\left| \theta_0^c \right| = 18° \pm \Delta\theta°, \tag{19}$$

where $\Delta\theta° = 180/(5N)$, which quantifies the uncertainty due to $\Delta\alpha^* = 0.2$. We can further estimate the corresponding critical separation angle θ_s for the PSP on the same side as

$$\theta_s^c (\text{PSP}) \approx \pm \left(90° - \left| \theta_0^c \right| - \frac{180°}{N} \right), \tag{20}$$

with (+) and (−) for the top and the bottom surfaces, respectively. Due to $x_\delta^{T,B}$ being asymmetric at off-principal orientations, the largest x_δ is the top shear layer for $N = 5n - 1, 5n - 2$; bottom for $N = 5n + 1, 5n + 2$; symmetric for $N = 5n$, n being integers. The calculated critical θ_s is plotted in Fig. 19. For a given N, only the side with the larger x_δ is marked. It is known from the experimental

measurement for $N = 12, 16$ at their principal orientations that C_D at $\alpha^* = 0$ is smaller than $\alpha^* = 1$ [17], and therefore this condition is marked in Fig. 19. Moreover, rotating clockwisely from $\alpha^* = 0$, $|\theta_0|$ approaches $18°$ from a smaller angle on the bottom surface first [17], and therefore these two cases are marked on the bottom surface. This also suggests that the true θ_s^c(PSP) would have a slightly smaller magnitude than the marked experimental values.

Equation (20) performs less well for large N, where the effect of θ_s^c fades away gradually and $x_\delta^{T,B}$ becomes α independent. Asymptotically, Eqs. (19) and (20) predict $|\theta_s^c| \approx 72°$ for the circular cylinder ($N \rightarrow \infty$), which is approximately $\approx 6° \sim 8°$ less than that found by flow visualization in Xu *et al.* [17] and $\approx 10°$ less than that reported in Jiang [44]. A recent experimental study [49] observed subtle separation (PSP) and reattachment (SSP) behavior on circular cylinders having a rough surface, which is equivalent to a polygon of very large but finite N. It indicates the true PSP to be $\approx 20°$ smaller than the reported value, albeit at a smaller Re.

Taking the limiting circular cylinder case into consideration, θ_s^c can be estimated by the empirical equation

$$\theta_s^c(\text{PSP}) \approx \pm 1.36[1 - \exp(-0.12N)]\left(\frac{180}{\pi}\right), \tag{21}$$

where the last term converts radian to degree. For $N \rightarrow \infty$, $\theta_s^c = 78°$. Neglecting $\pm \Delta\theta$ in Eq. (19), Eq. (12) suggests that the critical PSP is always on T_1 and with an SSP on T_0, whose angular positions are related by $\theta_s^c(\text{SSP}) = \theta_s^c(\text{PSP}) \mp (360/N)$. It can be seen from Table I that $\kappa \leqslant 0.35$ for all these SSPs.

IV. CONCLUSIONS

In this paper, incident flow around polygonal cylinders of side number $N = 5, 6, 7, 8$ is numerically studied using LES at Re $= 10^4$. In total, six equally spaced incidence angles are investigated, covering the entire incidence spectrum. This paper focuses on the flow separation points and the shear layer flapping motion, as well as their signature in the time mean flow fields and aerodynamic forces.

The separation behavior is studied in terms of instantaneous and time mean vorticity fields as well as the wall shear stress on the surface of the cylinders. An analytical formula for predicting the separation points on the polygons is derived and is found to be in good agreement with experimental data. A distinctive shear layer flapping motion can be observed at some incidence angles. The flapping motion strength varies monotonically for $N = 5$ and nonmonotonically for $N = 6, 7, 8$. It is a minimum when drag coefficient is a minimum and lift coefficient is a maximum. It is also found that this flapping motion results in the formation of temporarily (or permanently) reattached shear layers. It leads to the formation of SSPs on the cylinder, which can also be temporary.

It is found that the time mean shear layer penetration distance is a robust quantity with which to scale the flapping motion strength as well as the aerodynamic forces. Based on this, a wake deflection angle is proposed which universally scales the lift and drag coefficient and Strouhal number. This not only works for all cases tested as well as other polygonal cylinder data available in the literature, but also for the circular cylinder asymptotically. Finally, a universal critical separation angle is proposed, which corresponds to the maximum vortex shedding frequency and minimum drag and shear layer flapping motion strength. An empirical equation is provided for this critical condition which works reasonably well for $N \ll \infty$.

[1] C. H. Williamson, Vortex dynamics in the cylinder wake, Annu. Rev. Fluid Mech. **28**, 477 (1996).

[2] M. M. Zdravkovich, *Flow Around Circular Cylinders*, Fundamentals, Vol. 1 (Oxford University Press, 1997).

[3] M. Matsumoto, Vortex shedding of bluff bodies: A review, J. Fluids Struct. **13**, 791 (1999).

[4] M. C. Thompson, T. Leweke, and C. H. Williamson, The physical mechanism of transition in bluff body wakes, J. Fluids Struct. **15**, 607 (2001).

[5] A. Sohankar, C. Norberg, and L. Davidson, Simulation of three-dimensional flow around a square cylinder at moderate Reynolds numbers, Phys. Fluids **11**, 288 (1999).

[6] A. Sohankar, Flow over a bluff body from moderate to high Reynolds numbers using large eddy simulation, Computers & Fluids **35**, 1154 (2006).

[7] G. Iungo and G. Buresti, Experimental investigation on the aerodynamic loads and wake flow features of low aspect-ratio triangular prisms at different wind directions, J. Fluids Struct. **25**, 1119 (2009).

[8] R. Huang, B. Lin, and S. Yen, Time-averaged topological flow patterns and their influence on vortex shedding of a square cylinder in cross flow at incidence, J. Fluids Struct. **26**, 406 (2010).

[9] S. G. Prasath, M. Sudharsan, V. V. Kumar, S. Diwakar, T. Sundararajan, and S. Tiwari, Effects of aspect ratio and orientation on the wake characteristics of low Reynolds number flow over a triangular prism, J. Fluids Struct. **46**, 59 (2014).

[10] Z. Y. Ng, T. Vo, W. K. Hussam, and G. J. Sheard, Two-dimensional wake dynamics behind cylinders with triangular cross-section under incidence angle variation, J. Fluids Struct. **63**, 302 (2016).

[11] S. Yagmur, S. Dogan, M. H. Aksoy, I. Goktepeli, and M. Ozgoren, Comparison of flow characteristics around an equilateral triangular cylinder via PIV and large eddy simulation methods, Flow Measur. Instrum. **55**, 23 (2017).

[12] Y. Cao, T. Tamura, D. Zhou, Y. Bao, and Z. Han, Topological description of near-wall flows around a surface-mounted square cylinder at high reynolds numbers, J. Fluid Mech. **933**, A39 (2022).

[13] X. Tian and S. Li, Scientific measurements of disturbance on the prototype stands in a low speed wind tunnel (in chinese), Exp. Res. Aerodyn. **25**, 1 (2007).

[14] Z. W. Tian and Z. N. Wu, A study of two-dimensional flow past regular polygons via conformal mapping, J. Fluid Mech. **628**, 121 (2009).

[15] H. A. Khaledi and H. I. Andersson, On vortex shedding from a hexagonal cylinder, Phys. Lett. A **375**, 4007 (2011).

[16] Y. Lee, G. Zhou, and K. B. Lua, Two-dimensional numerical study of isotoxal-star polygonal cylinders in cross-flow, J. Wind Eng. Ind. Aerodyn. **188**, 125 (2019).

[17] S. Xu, W. Zhang, L. Gan, M. Li, and Y. Zhou, Experimental study of flow around polygonal cylinders, J. Fluid Mech. **812**, 251 (2017).

[18] Q.-Y. Wang, S.-J. Xu, L. Gan, W.-G. Zhang, and Y. Zhou, Scaling of the time-mean characteristics in the polygonal cylinder near-wake, Exp. Fluids **60**, 181 (2019).

[19] Q. Wang, L. Gan, S. Xu, and Y. Zhou, Vortex evolution in the near wake behind polygonal cylinders, Exp. Thermal Fluid Sci. **110**, 109940 (2020).

[20] E. Masoudi, L. Gan, and D. Sims-Williams, Large eddy simulation of incident flows around polygonal cylinders, Phys. Fluids **33**, 105112 (2021).

[21] S. F. Hoerner, Fluid-dynamic drag, practical information on aerodynamic drag and hydrodynamic resistance, Fluid-Dynamic Drag (1965), pp. 0–2, 2–8, available at http://ftp.demec.ufpr.br/disciplinas/TM240/Marchi/Bibliografia/Hoerner.pdf.

[22] B. Ahlborn, M. L. Seto, and B. R. Noack, On drag, Strouhal number and vortex-street structure, Fluid Dyn. Res. **30**, 379 (2002).

[23] M. M. Alam and Y. Zhou, Alternative drag coefficient in the wake of an isolated bluff body, Phys. Rev. E **78**, 036320 (2008).

[24] X.-Y. Lu and C. Dalton, Calculation of the timing of vortex formation from an oscillating cylinder, J. Fluids Struct. **10**, 527 (1996).

[25] M. Breuer, Numerical and modeling influences on large eddy simulations for the flow past a circular cylinder, Int. J. Heat Fluid Flow **19**, 512 (1998).

[26] M. Breuer, A challenging test case for large eddy simulation: High Reynolds number circular cylinder flow, Int. J. Heat Fluid Flow **21**, 648 (2000), Turbulence and Shear Flow Phenomena 1.

[27] S. Atluri, V. Rao, and C. Dalton, A numerical investigation of the near-wake structure in the variable frequency forced oscillation of a circular cylinder, J. Fluids Struct. **25**, 229 (2009).

[28] M. Breuer, G. De Nayer, M. Münsch, T. Gallinger, and R. Wüchner, Fluid-structure interaction using a partitioned semi-implicit predictor-corrector coupling scheme for the application of large-eddy simulation, J. Fluids Struct. **29**, 107 (2012).

[29] S. Kim, P. A. Wilson, and Z.-M. Chen, Numerical simulation of force and wake mode of an oscillating cylinder, J. Fluids Struct. **44**, 216 (2014).

[30] S. Kim, P. A. Wilson, and Z.-M. Chen, Effect of turbulence modelling on 3-D LES of transitional flow behind a circular cylinder, Ocean Eng. **100**, 19 (2015).

[31] R. Wang, S. Cheng, and D. S. Ting, Effect of yaw angle on flow structure and cross-flow force around a circular cylinder, Phys. Fluids **31**, 014107 (2019).

[32] R. Wang, S. Cheng, and D. S.-K. Ting, Numerical study of roundness effect on flow around a circular cylinder, Phys. Fluids **32**, 044106 (2020).

[33] A. Travin, M. Shur, M. Strelets, and P. Spalart, Detached-eddy simulations past a circular cylinder, Flow, Turbul. Combust. **63**, 293 (2000).

[34] A. G. Kravchenko and P. Moin, Numerical studies of flow over a circular cylinder at $Re_D = 3900$, Phys. Fluids **12**, 403 (2000).

[35] D. F. L. Labbé and P. Wilson, A numerical investigation of the effects of the spanwise length on the 3-D wake of a circular cylinder, J. Fluids Struct. **23**, 1168 (2007).

[36] S. Wornom, H. Ouvrard, M. V. Salvetti, B. Koobus, and A. Dervieux, Variational multiscale large-eddy simulations of the flow past a circular cylinder: Reynolds number effects, Computers & Fluids **47**, 44 (2011).

[37] K. Zhang, H. Katsuchi, D. Zhou, H. Yamada, and Z. Han, Numerical study on the effect of shape modification to the flow around circular cylinders, J. Wind Eng. Ind. Aerodyn. **152**, 23 (2016).

[38] J. Smagorinsky, General circulation experiments with the primitive equations: I. The basic experiment, Mon. Weather Rev. **91**, 99 (1963).

[39] C. Fureby, G. Tabor, H. Weller, and A. Gosman, A comparative study of sub-grid scale models in homogeneous isotropic turbulence, Phys. Fluids **9**, 1416 (1997).

[40] E. R. Van Driest, On turbulent flow near a wall, J. Aeronaut. Sci. **23**, 1007 (1956).

[41] S. B. Pope, Ten questions concerning the large-eddy simulation of turbulent flows, New J. Phys. **6**, 35 (2004).

[42] J.-C. Lin, J. Towfighi, and D. Rockwell, Instantaneous structure of the near-wake of a circular cylinder: On the effect of reynolds number, J. Fluids Struct. **9**, 409 (1995).

[43] S. Dong and G. E. Karniadakis, Dns of flow past a stationary and oscillating cylinder at Re = 10000, J. Fluids Struct. **20**, 519 (2005).

[44] H. Jiang, Separation angle for flow past a circular cylinder in the subcritical regime, Phys. Fluids **32**, 014106 (2020).

[45] P. Bearman, On vortex street wakes, J. Fluid Mech. **28**, 625 (1967).

[46] A. Roshko, On the Drag and Shedding Frequency of Two-Dimensional Bluff Bodies, Tech. Rep. No. 3169, California Institute of Technology, 1954.

[47] A. Roshko, On the wake and drag of bluff bodies, J. Aeronaut. Sci. **22**, 124 (1955).

[48] A. Sohankar, S. Mohagheghian, A. A. Dehghan, and M. D. Manshadi, A smoke visualization study of the flow over a square cylinder at incidence and tandem square cylinders, J. Visualization **18**, 687 (2015).

[49] C. Sun, T. Zhou, H. An, H. Zhu, and L. Cheng, Experimental studies on wake structures of a circular cylinder with different surface roughness heights, Int. J. Heat Fluid Flow **94**, 108941 (2022).